Article

Adaptive multisensor data fusion for acoustic emission source localization in noisy environment

Ehsan Dehghan Niri, Alireza Farhidzadeh and Salvatore Salamone

Abstract
This article proposes an adaptive multisensor fusion algorithm for acoustic emission source location in isotropic plate-like structures in noisy environments. Overall, the approach consists of the following four main stages: (a) feature extraction, (b) sensor selection based on a binary hypothesis testing, (c) sensor weighting based on a well-defined reliability function, and (d) estimation of the acoustic emission source location based on the extended Kalman filter. The performance of the proposed algorithm is validated through pencil lead breaks performed on an aluminum plate instrumented with a sparse array of piezoelectric sensors. Two experimental setups have been used to simulate a highly noisy environment. In the first setup, the experimental signals have been artificially corrupted with different levels of noise generated by a Monte Carlo simulation. In the second setup, two piezoelectric transducers have been used to continuously generate high-power white noise during testing. The results show the capability of the proposed algorithm for inflight structural health monitoring of metallic aircraft panels in highly noisy operational situation.

Keywords
Acoustic emission, multisensor fusion, extended Kalman filter, binary hypothesis test, Lamb waves, structural health monitoring

Introduction

In the past two decades, significant efforts have been made toward the development of integrated structural health monitoring (SHM) systems in order to increase the safety of aircraft systems[1–3] and reduce life-cycle costs.[4] The techniques based on sparse arrays of piezoelectric sensors, which have the capability of transmitting and receiving Lamb waves are among the most promising candidates. Damage location using Lamb waves can be achieved either by an "active–passive" approach or by a "passive-only" approach. In the "active–passive" approach, diffractions of piezoelectrically actuated waves can be used to locate existing damage in a postmortem mode.[5,6] In the "passive-only" approach, growing damage (e.g. fatigue cracks) or sudden impacts can be located by monitoring acoustic emissions (AEs) in a real-time mode.[7–15] This article focuses on a "passive-only" approach using a sparse array of piezoelectric transducers. Traditionally, the damage or impact location is based on time-of-flight (TOF) triangulation of wave measurements taken at multiple receiving points. This technique works very

well when the wave velocity (V_g) in the test material and the arrival time (t_i) of the signal at all three sensor locations are known. The damage or impact location is identified by drawing three circles of radii (R_i), whose centers coincide with the three sensor locations. The radius R_i is obtained by multiplying the time of arrival of the signal (t_i) with the wave velocity (V_g). The intersection point of these three circles is the damage location (Figure 1(a)). However, the TOF and wave velocity are two uncertain parameters. In general, uncertainties can be caused by random and systematic errors. The random errors are caused by unknown and unpredictable changes in the TOF measurements, including instrumentation noise, temperature changes,

Smart Structures Research Laboratory, Department of Civil, Structural and Environmental Engineering, State University of New York at Buffalo (UB), NY, USA

Corresponding author:
Salvatore Salamone, Smart Structures Research Laboratory, Department of Civil, Structural and Environmental Engineering, State University of New York at Buffalo (UB), NY 14260, USA.
Email: ssalamon@buffalo.edu
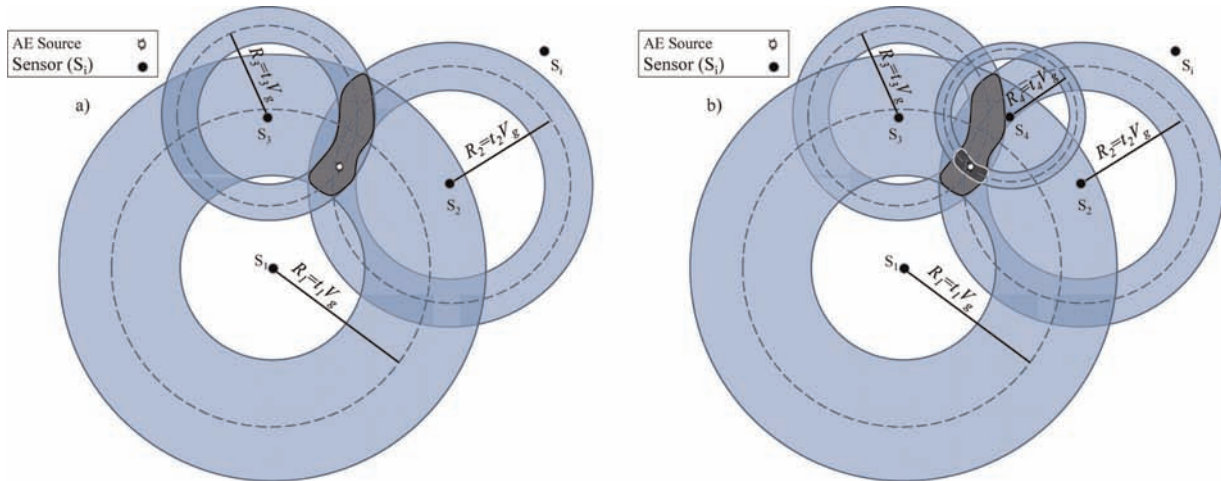
Figure 1. AE source location likelihood area: (a) three sensors with different uncertainties and (b) four sensors with different uncertainties.
AE: acoustic emission.

and so on.[16–21] The systematic errors are mostly caused by the digital signal-processing technique used for analyzing the time waveforms.[22,23] As a result, rather than the damage being located at a single point at the intersection of the circles, it can be located anywhere in the dark overlapped region at the intersection of the rings around the sensor locations (Figure 1(a)). The ring's width represents the uncertainty in the measured distance as a result of TOF and/or wave velocity uncertainties. It should be noted that, uncertainties can be directionally dependent on anisotropic structures. In general, the lower the signal-to-noise ratio (SNR), the higher the ring's width (i.e. higher uncertainty in TOF measurements). To overcome these limitations, model-based approaches[24] have been proposed for impact identification in simple structures. In these methods, the location and type of impact in a numerical model are iteratively changed until the predicted responses match the measured responses. For the damage/impact location in more complex structures, where accurate model-based predictions may not be possible, artificial neural networks have been proposed.[25,26] The time reversal approaches have been used to accurately find the source location in complex structures.[27–30] Sohn et al.[28] and Park et al.[29] have shown that the time reversal algorithm is able to efficiently localize the impact in isotropic and anisotropic plate-like structures. However, neural networks and time reversal approaches require an extensive number of training observations prior to deployment, making these methods quite onerous from a computational or data storage point of view. Kundu et al.[8] proposed an alternative method based on optimizing an objective function to find the impact location in isotropic and anisotropic plates. However, the

proposed objective function in that reference had the inherent problem of multiple singularities, which was overcome in Kundu et al.[31] by modifying the objective function. The optimization technique was further improved by Hajzargarbashi et al.[32] Kundu et al.[33] proposed a technique to locate acoustic source in large anisotropic plates that does not require the knowledge of the direction-dependent velocity profile or a dense array of sensors. In Gaul[34] and Gaul et al.,[35] the nonlinear least squares optimization adopting the Gauss–Newton method was proposed to determine the location, time lag, and velocity of "synthetic" AE signals. Ciampa and Meo[13] used Newton's iterative method to calculate the coordinates of the impact location and the wave velocity. A genetic algorithm (GA) for the optimization of an objective function based on the modified triangulation methodology was proposed by Coverley and Staszewski.[36] Dehghan Niri and Salamone[14] proposed a probabilistic approach for source localization in the isotropic plate-like structures based on the extended Kalman filter (EKF) theory. However, they just considered the systematic errors in the TOF measurements, without taking into account the random errors caused by the unknown and unpredictable changes in the measurements, including environmental noise effect. Here, an alternative framework, based on a multisensor data fusion algorithm, is proposed for the real-time AE source localization and wave velocity estimation in the isotropic plate-like structures, in a highly noisy environment. The multisensor data fusion is a fairly young field, which has mainly been considered and developed in military target tracking and autonomous robotics.[37–39] Multisensor data fusion is a process similar to the methods humans use to integrate data from multiple sources
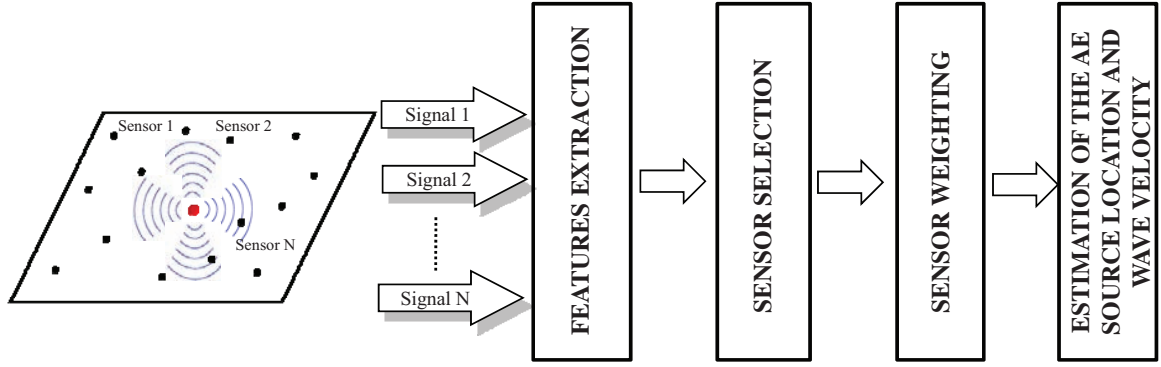
Figure 2. Schematic architecture of proposed adaptive multisensor fusion algorithm.

and senses to make decisions. In addition to the statistical advantage gained by combining same-source data (e.g. obtaining an improved estimate of physical phenomena via redundant observations),[14] the use of multiple sensors may increase the accuracy with which a quantity (e.g. damage location) can be observed and characterized (Figure 1(b)).

In this process, the accuracy of the data is the most crucial aspect. In fact, the fusion of inaccurate data, such as "noisy" data, can badly affect the estimation of the damage location. Therefore, each sensor's information (i.e. TOF measurements) cannot be used equally. In fact, the information extracted from each sensor depends on the actual SNR, which is related to several factors, including intensity of the damage event, environmental and instrumentation noise, attenuation, and so on. In the proposed approach, the sensors with higher SNR are given more weight, and those with smaller SNR are given less weight. For example, in the configuration shown in Figure 1(b), the sensor 4 should have more weight than the other sensors in the AE source location estimation. A schematic diagram of the proposed algorithm is shown in Figure 2.

In particular, the algorithm begins by a feature extraction from each recorded signal. These features consist of dominant frequency (f_i), TOF_i, peak amplitude of the signal envelope (A_{max}), and standard deviation of the actual noise level (σ_n). Next, a decision is made to use or disregard data from a given sensor, based on a binary hypothesis test. Then, the information from the remaining sensors is weighted according to a well-defined reliability function. Finally, the weighted data are used as input to an EKF algorithm, which iteratively estimates (a) the AE source location and (b) the wave velocity.

AE source location

Assuming an arbitrary Cartesian coordinate system, the AE source is at unknown coordinates (x_s, y_s) in the plane of the plate and the sensors are located at (x_i, y_i),
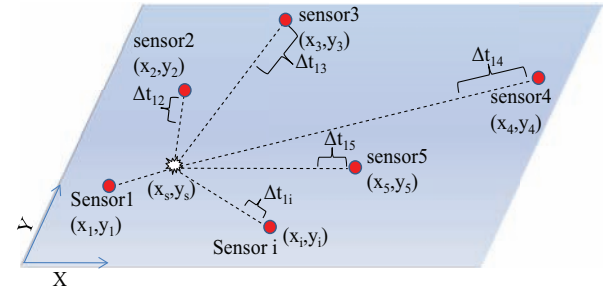
Figure 3. AE source location and sparse array of *n* piezoelectric sensors.
AE: acoustic emission.

as shown in Figure 3. It is well known that given the wave velocity of a particular Lamb wave mode, at least three sensors are necessary to locate an AE source in the plate-like structures. If t_m is the travel time or TOF to reach the first sensor (master sensor), and Δt_{mi} are the time difference between master sensor and the *i*th sensor, the following equations can be obtained

$$(x_m - x_s)^2 + (y_m - y_s)^2 - (t_m V_g)^2 = 0 \qquad (1)$$

$$(x_i - x_s)^2 + (y_i - y_s)^2 - [(t_m + \Delta t_{mi})V_g]^2 = 0 \qquad (2)$$

where V_g is the group velocity of the particular Lamb wave mode, which is a function of the product of the frequency *f* and the plate thickness *d*

$$V_g = F(fd) \qquad (3)$$

By knowing the properties of the plate, mass density ρ, thickness *d*, Young's modulus *E*, and Poisson's ratio ν, V_g can be calculated by the *Rayleigh–Lamb equations*.[40] Combining equations (1) and (2), the following equation can be derived

$$\Delta t_{mi} = \frac{\sqrt{(x_i - x_s)^2 + (y_i - y_s)^2} - \sqrt{(x_m - x_s)^2 + (y_m - y_s)^2}}{V_g}$$

$$(4)$$

In general, the difference between the TOF of the master sensor to different sensors (Δt_{mi}) is used to solve this set of nonlinear equations with unknowns $\mathbf{X} = (x_s, y_s, V_g)$. It should be noted that the master sensor is defined as the first sensor triggered by the AE source (i.e. the sensor closest to the AE source). However, as mentioned in the previous section, several sources of error in the TOF measurements (i.e. dispersion, noise, and temperature) can affect the accuracy of this solution. In this work, to take into account the uncertainty in TOF, the arrival time t_i are treated as mutually independent Gaussian random variables. Also considering wave velocity and location uncertainties, the unknowns x_s, y_s, and V_g are initially considered as mutually independent Gaussian random variables. It should be noted that the arrival time t_i and the unknowns x_s, y_s, and V_g are not independent since those are related by equation (4). Based on this assumption, the probability density function of the time difference Δt_{mi} can also be defined as a Gaussian random variable[41] with mean and variance defined as

$$\Delta t_{mi} = t_i - t_m, \quad \sigma^2_{\Delta t_{mi}} = \sigma^2_{t_i} + \sigma^2_{t_m} \qquad (5)$$

The determination of time differences Δt_{mi} and the related uncertainties in highly noisy environment is discussed in the "Statistical characterization of time of flight measurement" section. In this probabilistic framework, an EKF approach is used for the optimal estimation of the state vector $X = (x_s, y_s, V_g)$.

Statistical characterization of TOF measurement

The errors in the TOF measurements of Lamb waves are strongly dependent on the SNR, as has been qualitatively discussed in the "Introduction" section. In general, the lower the SNR, the higher the uncertainty in the TOF measurement. This section presents a statistical characterization of TOF errors for different noise levels. Toward this end, flexural Lamb waves are first modeled analytically to predict the acoustic field in an isotropic plate-like structure generated by the AE sources. Then, the simulated signals are corrupted artificially with different noise levels; using a Monte Carlo simulation, the statistical distribution of the TOF error for each level of noise is calculated.

Lamb wave model due to a point source excitation

In the plate-like structures, the following two fundamental Lamb wave modes can propagate: symmetric (S_n) and antisymmetric (A_n). The displacements of the symmetric modes occur in the direction of wave propagation (i.e. extensional modes), while the antisymmetric modes have displacements transverse to the wave propagation direction (i.e. flexural modes). In this article, it is assumed that only the lowest order flexural mode (A_0) is the dominant mode.[42] The Lamb waves have been modeled by Ditri's technique, with normal point excitation on the surface of the plate.[43] In particular, to model the total out-of-plane surface displacements u_z associated with an input of finite duration $f(t)$, a Fourier transform is used to decompose the input signal into its different frequency components, $f(\omega)$. The input, for pencil lead break simulations, has been assumed as a one-cycle tone burst enclosed in a Hanning window and a center frequency of 1 MHz.[44] The out-of-plane displacement as a function of time and distance from the source is given by[43]

$$u_z(r, t) = \int f(\omega) \sum_m E_m(\omega) H_0^1(k_m r) \exp(-i\omega t) d\omega \qquad (6)$$

where t is the time, r is the distance from the point source, k_m is the wave number of the excited Lamb mode (m) corresponding to ω, which can be calculated through the phase velocity V_{ph}^m ($k_m = \omega / V_{ph}^m$), and i is the imaginary unit; and $E_m(\omega)$ is the excitability function for circular crested waves that depend on the angular frequency ω and excited mode m. The spatial variation in a circular crested Lamb wave model is expressed by the Hankel function of first kind H_0^1. Using Viktorov's method,[45] the excitability can be computed. The excitability of a mode is totally governed by the amount of out-of-plane displacement of the mode due to a normal point excitation. In this work, in modeling Lamb waves generated by pencil lead breaks, it is assumed the A_0 mode is the dominant mode.[46] The phase velocity (V_{ph}) for different modes and excitability $E(\omega)$ just for the fundamental mode A_0, are shown in Figure 4.

Equation (6) enables the surface displacement to be plotted as a function of both distance and time, when the plate is excited by a finite duration input at a point. Figure 5 shows some of the modeled signals at different distances from the source (i.e. pencil lead break). The duration and the sampling frequency are fixed to 0.4 ms and 3 MHz, respectively. All the signals are normalized to the maximum response at 5 cm. These signals will be corrupted artificially with different noise levels (generated by a Monte Carlo simulation), to determine the statistical distribution of the extracted features, including TOF and peak amplitude of the signal envelope.

TOF measurement

Several methods have been proposed in the literature for the TOF measurement of acoustic signals, including threshold crossing, coloration methods, wavelet transform, and curve fitting approaches.[47] In this work, the
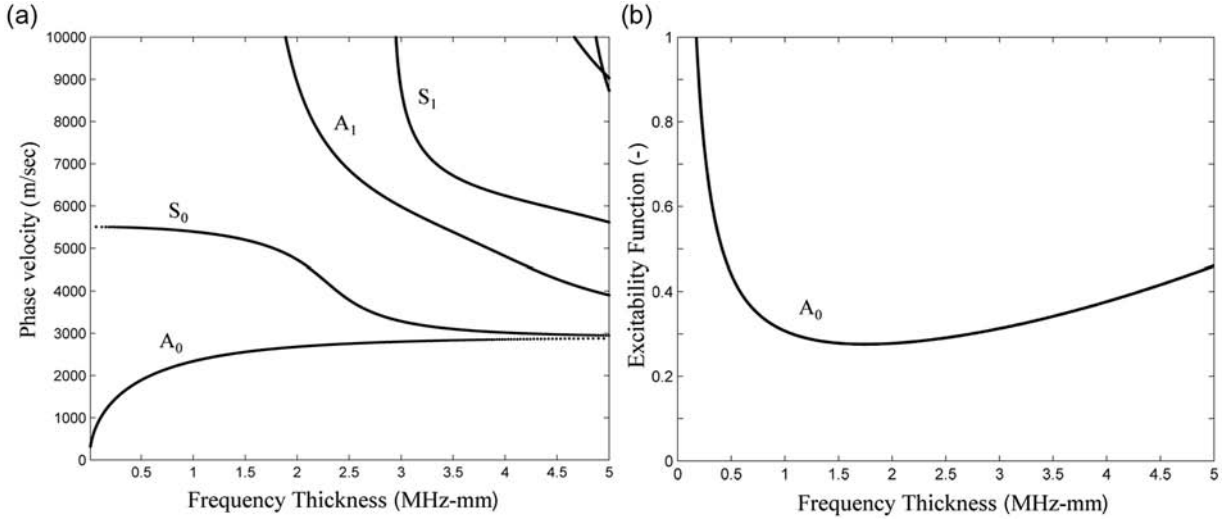
Figure 4. (a) Dispersion curves for circular crested Lamb waves in aluminum plate and (b) excitability function for the fundamental mode A_0 in aluminum plate.
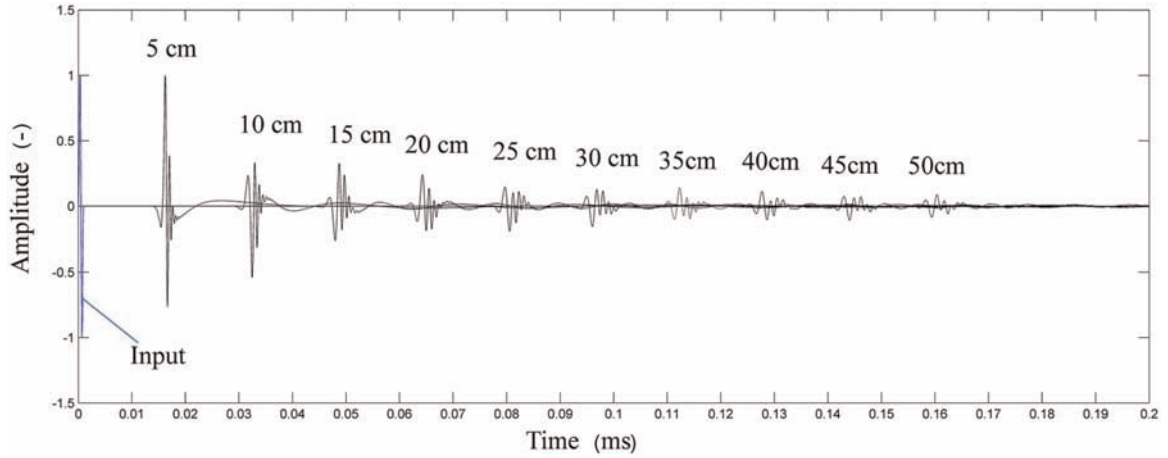
Figure 5. Signal simulation for one-cycle sinusoidal input in one point with center frequency of 1 MHz.

TOF has been estimated for both experimental and numerical signals by the peak amplitude of the signal envelope.[36] The envelope can be calculated using the definition of analytic signal $x_A(t)$ of a real signal $x(t)$ as follows

$$x_A(t) = x(t) + ix_H(t) \tag{7}$$

where i is the imaginary unit and $x_H(t)$ is the Hilbert transformation of $x(t)$ defined as

$$x_H(t) = \frac{1}{\pi} \int_{-\infty}^{+\infty} x(\tau) \frac{1}{t - \tau} d\tau \tag{8}$$

The magnitude of the analytical signal, which is identical to the magnitude of the real signal, is called an envelope

$$A(t) = \sqrt{x(t)^2 + x_H(t)^2} \tag{9}$$

The time instant in which the envelope of the signal reaches its maximum (A_{max}), is considered as the TOF. Some envelopes of the simulated signals and the corresponding nominal TOFs are shown in Figure 6.

TOF error of noisy data

Several methods have been investigated to analyze the error in the TOF measurements of acoustic signals in random noise, including threshold crossing[23] and cross correlation.[47,48] In this work, the noise is modeled as an additive zero-mean Gaussian random process with variance σ_n^2. The ratio between the peak amplitude of the signal envelope (A_{max}) and the standard deviation of the noise (σ_n) is used as a representative feature of the
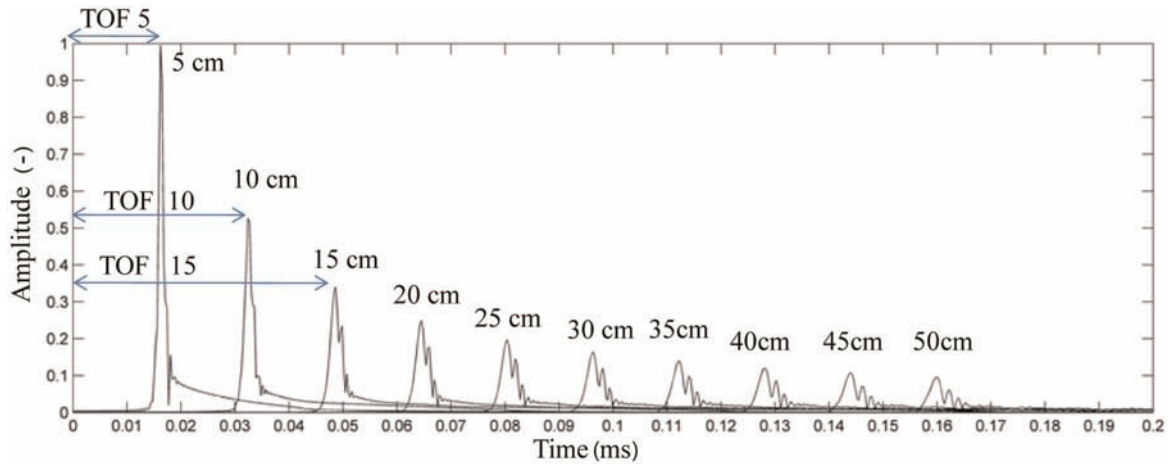
Figure 6. Envelope of modeled signals and nominal TOF.
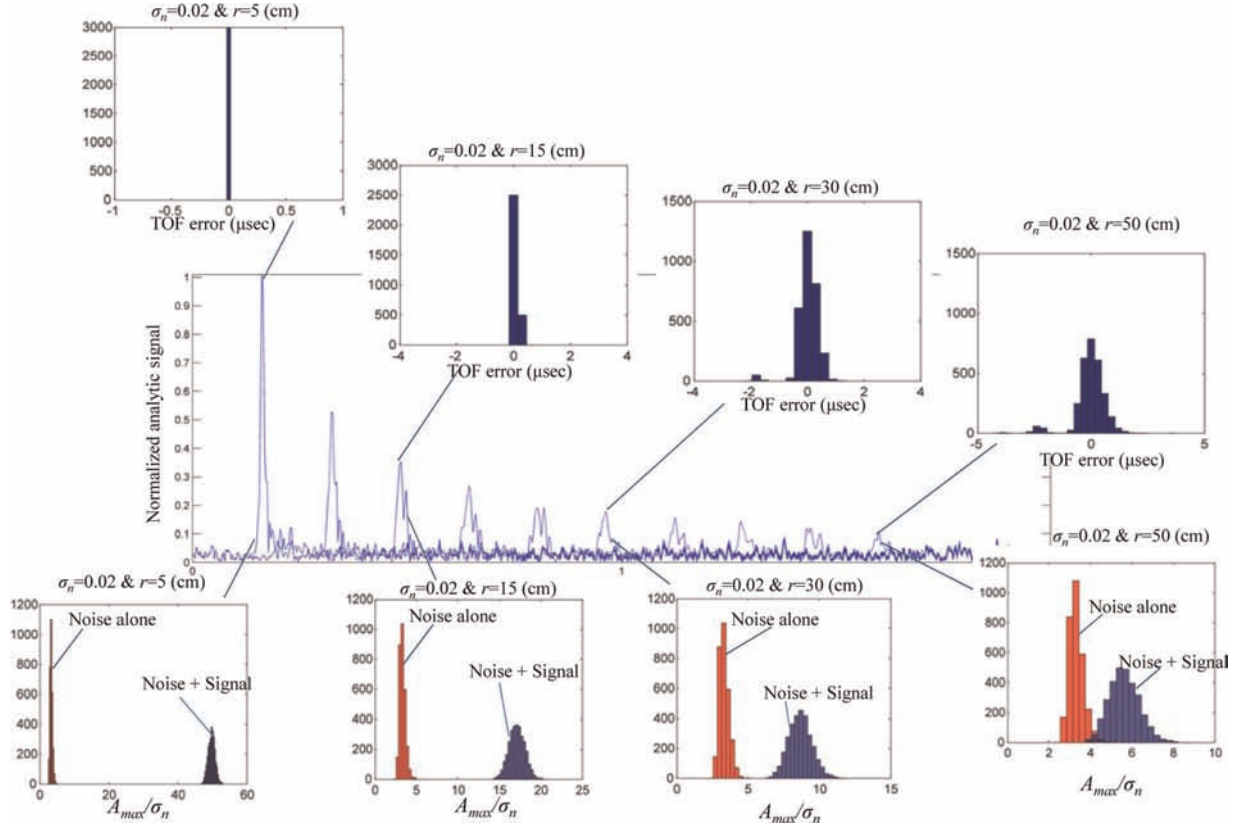TOF: time of flight.
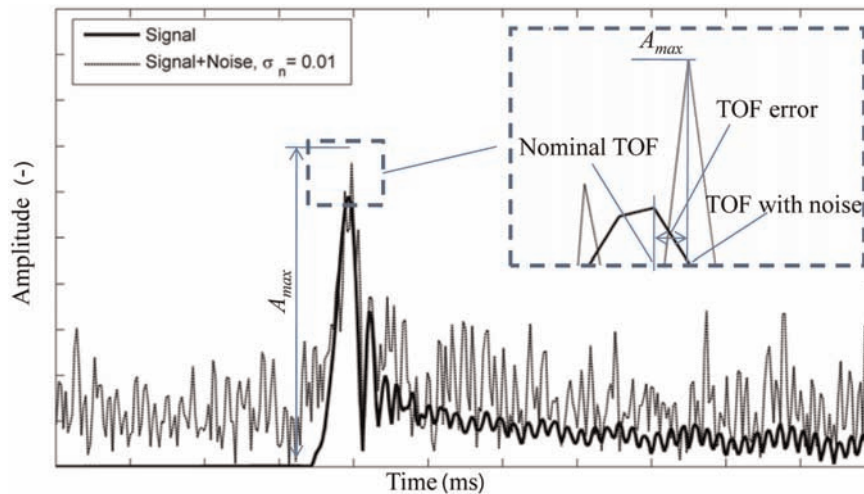
Figure 7. Definition of TOF error.
TOF: time of flight.

SNR. In general, the level of the background noise in real applications can be estimated by the root mean square (RMS) value of a predetermined portion of the signal before the first arrival. In this work, the TOF error is defined as the difference between the nominal TOF captured from predicted signals using equation (6) (i.e. noise-free signals) and the TOF extracted from the predicted signals artificially corrupted with noise, as shown in Figure 7. In particular, a Monte Carlo simulation has been used to corrupt the predicted signal with noise with a standard deviation of 0.01.

To capture the statistic distribution of both features (i.e. TOF error and (A_{max}/σ_n)), a predicted signal at a given distance r has been corrupted 3000 times with a fixed noise level using a Monte Carlo simulation. For each simulation, the two features have been extracted. Then, histograms have been constructed to predict the distribution of the TOF error and A_{max}/σ_n. This procedure has been repeated for different distances (r) and different noise levels (σ_n). For the sake of clarity, Figure 8 shows the envelope of the predicted signal at different distances with a superimposed noise level of $\sigma_n = 0.02$; in addition, histograms for some signals (i.e. 5, 15, 30, and 50 cm) are indicated.

It can be observed that as the SNR decreases, the distribution of A_{max}/σ_n for signal plus noise gets closer to that of noise alone; as a result, the detection of the envelope becomes more unlikely. In addition, as the SNR decreases, the standard deviation of the TOF error (σ_t) increases. In this work, the standard deviation

**Figure 8.** Monte Carlo analysis.
TOF: time of flight.
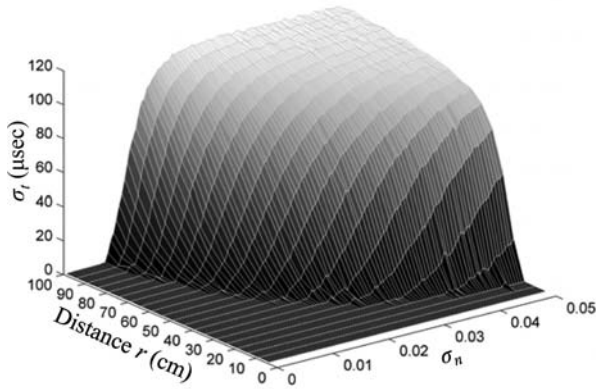
Figure 9. TOF uncertainty versus distance and noise level.
TOF: time of flight.

of the TOF error (σ_t) is used as a measure of the TOF uncertainty. The variation of σ_t versus distance and noise level is shown in Figure 9. Note that the further a particular sensor is from the AE source, the more unreliable data (TOF) are extracted from it. In the "Sensor selection based on binary hypothesis testing" section, a binary decision test is proposed to neglect the most unreliable sensors.

Sensor selection based on binary hypothesis testing

Although using more data from a sparse array of sensors leads to more accurate results, the fusion of inaccurate data can adversely affect the interpretation of the physical phenomenon of interest (i.e. damage/impact location). Thus, it would be beneficial in making a decision as to whether to use or disregard data provided by a given sensor. Toward this end, in this section, a binary hypothesis testing is used to classify between a signal and noise based on the received signal. The binary hypothesis testing are procedures useful for developing decision-making algorithms. In particular, these procedures are used to determine whether a measurement is consistent with one of the two states (H_0 and H_1) called hypotheses. The hypotheses H_0 and H_1 are sometimes referred to as the null and the alternative hypotheses, respectively.[49] In this context, if y_i is the signal received by a given sensor i, the measurements under the two different hypotheses are given by

$$y_i = \begin{cases} S + n_i & H_1 \\ n_i & H_0 \end{cases} \qquad (10)$$
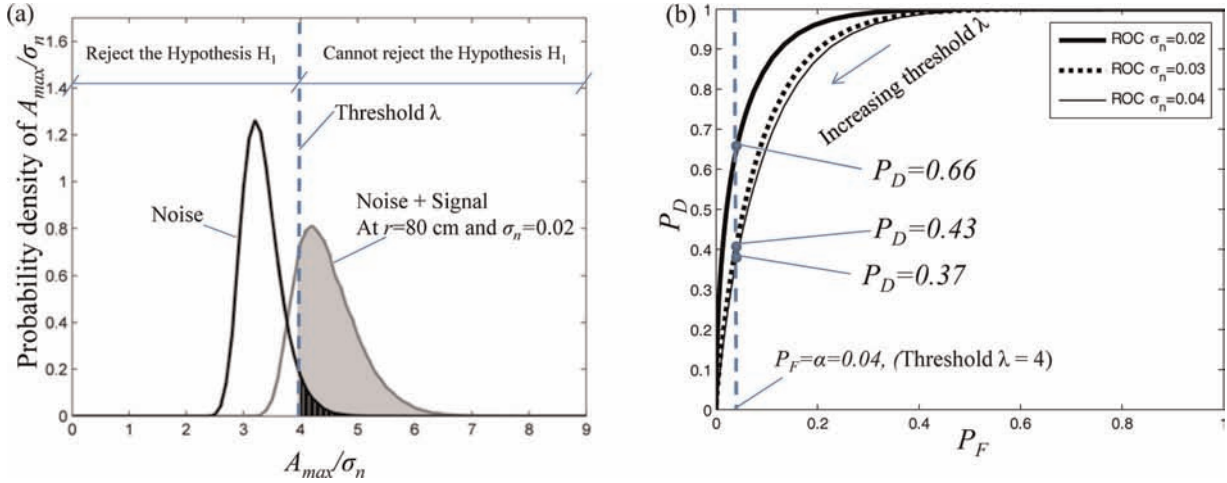
Figure 10. (a) A_{max}/σ_n probability density function of noise and signal plus noise and (b) ROC for signal at r = 80 cm. ROC: receiver operating characteristic.

where H_1 denotes the "*signal-present*" hypothesis and H_0 is the null hypothesis (i.e. no signal present); S is an arbitrary deterministic signal; and n_i is zero-mean, Gaussian noise with variance σ_n^2. It is assumed that the feature (A_{max}/σ_n) extracted from each signal (y_i) is a sufficient statistic and contains all the required information needed to make a decision. Therefore, the task is to decide in favor of H_0 or H_1 on the basis of the measurements (A_{max}/σ_n). In testing H_0 versus H_1, there are two types of errors that can be made as follows: H_0 can be falsely rejected or H_1 can be falsely rejected. The first of these two error types is called a *false alarm* (i.e. the signal is said to be present when it is not). The second type is called a *miss* (i.e. the signal is said to be absent when it is present). The terms "*false alarm*" and "*miss*" come from radar problems in which H_0 and H_1 usually represent the absence and presence of a target, respectively. The probability of the first type of error is known as the false alarm probability and is denoted as P_F; similarly, the probability of the second type of error is called the miss probability P_M. However, in discussing the latter quantity, it is more common to refer to the probability of detection, $P_D = 1 - P_M$. These probabilities can be obtained by the conditional densities, $P(A_{max}/\sigma_n|H_0)$ and $P(A_{max}/\sigma_n|H_1)$, that reveal how the extracted feature (A_{max}/σ_n) is distributed under the two respective hypotheses. In this work, a Monte Carlo simulation has been used to calculate these conditional probabilities, considering as deterministic signal (S) the Lamb wave modeled as described in the "Lamb wave model due to a point source excitation" section for r = 80 cm. In Figure 10(a), the probability density for noise alone (i.e. $P(A_{max}/\sigma_n|H_0)$) is plotted along with that for signal and noise (i.e. $P(A_{max}/\sigma_n|H_1)$). A threshold λ is shown. The gray area under the curve for signal plus

noise represents the P_D, while the double-crosshatched black area under the curve for noise alone represents the P_F. Obviously, if the threshold is increased to reduce the probability of false alarm, the probability of detection will also be reduced.

The design of a test for H_0 versus H_1 involves a trade-off between the probabilities of the two types of errors since one can be made arbitrarily small at the expense of the other. The *Neyman–Pearson* test criterion for making this trade-off is to place a bound on the false alarm probability, that is

$$P_F = \int_{\lambda}^{+\infty} P\left(\frac{A_{max}}{\sigma_n}\Big|H_0\right) dr = \alpha \qquad (11)$$

Solving this equation for a fixed value of α, the decision threshold (λ) can be calculated. The decision based on the *Neyman–Pearson* test is to accept H_0 (i.e. neglecting the sensor data) if $A_{max}/\sigma_n < \lambda$ or H_1 (i.e. use the sensor data) if $A_{max}/\sigma_n > \lambda$. To describe the performance of the decision test, the receiver operating characteristics (ROCs), which is nothing more than a plot of P_D versus P_F as threshold λ is varied, is shown in Figure 10(b) for different levels of noise. It can be observed that for a given value of α (i.e. for a given threshold λ), the level of noise strongly affects the detection performance of a given sensor; in particular, the higher the noise, the lower the detection performance. This threshold will be fixed in this application in the "Results and discussion" section. In addition, it should be pointed out that if the number of remaining sensors is less than 4, then to solve the set of nonlinear equations described in the "AE source location" section (equation (4)), the four sensors that have the

largest ratio (A_{max}/σ_n) will have to be used. A detailed review of the signal detection theory is beyond the scope of this article and the readers may refer to Trees[49] for more information.

Sensor weighting

As mentioned in the previous section, in data fusion processes, the accuracy of the data is the most crucial aspect. In fact, the fusion of inaccurate data, such as "noisy" data, can badly affect the estimation of the damage location. Therefore, each sensor's information (e.g. TOF measurements) cannot be used equally. In this work, it is proposed to achieve an optimal data fusion by assigning weighting factors to each sensor's information, according to the standard deviation of the TOF error (σ_t). In particular, the sensors with higher SNRs (i.e. with smaller σ_t) are given more weight and those with smaller SNRs (with larger σ_t) are given less weight. As a result, the determination of weighting factors is related to the estimation of the standard deviation of the TOF error (σ_t) of each sensor. In Figure 8, it can be observed that a relationship exists between the distribution of the extracted feature (A_{max}/σ_n) for signal plus noise and σ_t; in particular, as the distribution of A_{max}/σ_n for signal plus noise gets closer to that of noise alone, the σ_t becomes larger. Therefore, the mean value of the distribution of A_{max}/σ_n can be used for signal plus noise, calculated for different noise levels and different distances, and correlated it with σ_t. The results of this procedure are shown in Figure 11. The exponential curve used to fit the data is used to define a reliability function as follows

$$\sigma_t = 7642 e^{-1.069\left(\frac{A_{max}}{\sigma_n}\right)} \qquad (12)$$

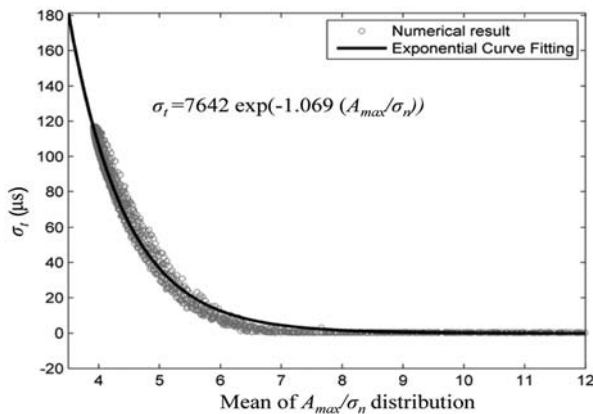Equation (12) is used in the proposed adaptive multisensor fusion algorithm to weight the contribution of

each data sensor. It should be pointed out that the equation (12) is not general, but it depends on the signal processing techniques used for the TOF measurements; in fact, these techniques have a different sensitivity to the noise level. However, in general, a decreasing SNR leads to increasing TOF measurement uncertainty;[50] this fact is clearly considered in this equation. Thus, when there is no such a function for the specific signal processing and configuration, using this equation as a primary function for weighting each sensor data in a highly noisy environment is recommended because it changes the contribution of each sensor relative to the other sensors (its absolute value is not as important as its relative value). In particular, the proposed approach to perform a multisensor data fusion is based on the EKF theory.

EKF

In general, a Kalman filter (KF) is a recursive data processing algorithm that estimates the *state* of a noisy dynamic system.[51] In this article, the *state* of a system is used to mean a vector X consisting of n variables describing some interesting properties of the system. To estimate the state, a KF processes all available measurements, both accurate and inaccurate. It is noteworthy that the KF belongs to the Bayesian inference-based estimators that have been widely used in SHM.[52] The KF has been extensively used in a wide range of applications due to its simplicity, optimality, robustness, sensor fusion ability, and capability of filtering out the uncertainties due to the mathematical model and measurements.[51,53–55] In general, the KF is a two-step process as follows: (a) *state prediction* according to a mathematical model and (b) *correction of the state* according to the measurements collected by the sensors. More specifically, in the prediction step, the KF estimates the state of the system at a given time instant and then obtains a feedback control in the correction step, by incorporating a new measurement result into the a priori estimate to gain an improved a posteriori estimate. Although the underlying approach is very promising, there is a critical limitation. In fact, the KF assumes that the system and measurements are adequately modeled by a linear dynamic system. The EKF is similar to the KF, but it can be used in nonlinear systems with linearization using first-order Taylor series expansion.[51] For this reason, the EKF has been used to handle the set of nonlinear equations (see equation (4)). In this work, the *state* of the system X consists of three parameters, namely, the AE source location (x_s, y_s) and the wave velocity V_g. Given a sparse array of N sensors, the time differences Δt_{mi} between the ith sensor and the master sensor represent the measurement data

Figure 11. Reliability function.

vector $\boldsymbol{Z} = [\Delta t_{mi}]_{(N-1)}$, $N \geq 4$. The *state* of the system $\boldsymbol{X}$ is related to the measurement vector $\boldsymbol{Z}$ through the nonlinear measurement function h defined in equation (4). The key idea underlying the proposed approach is that the AE source location can be considered as an unmovable (static) or slowly fluctuating point. Under this assumption, the EKF algorithm can be simplified as follows[14,15]

$$\hat{\boldsymbol{Z}}_k = h(\hat{\boldsymbol{X}}_{k-1}) \tag{13}$$

$$\hat{\boldsymbol{X}}_k = \hat{\boldsymbol{X}}_{k-1} + \bar{\boldsymbol{K}}_k(\boldsymbol{Z} - \hat{\boldsymbol{Z}}_k) \tag{14}$$

$$\hat{\boldsymbol{P}}_k = \left(\boldsymbol{I} - \bar{\boldsymbol{K}}_k\boldsymbol{H}_k\right)\hat{\boldsymbol{P}}_{k-1} \tag{15}$$

$$\boldsymbol{H}_k = \left.\frac{\partial h(\boldsymbol{X})}{\partial \boldsymbol{X}}\right|_{\boldsymbol{X} = \hat{\boldsymbol{X}}_{k-1}} \tag{16}$$

$\hat{\boldsymbol{Z}}_k$ is the predicted measurement vector in the kth step according to state estimation $\hat{\boldsymbol{X}}_{k-1}$ in the $(k-1)$th step using the nonlinear measurement function (h) defined in equation (4); this equation predicts difference in the TOFs or components of measurement vector based on the estimated state vector including location and wave velocity. $\hat{\boldsymbol{X}}_k$ is the estimated states in the kth step derived by correcting the estimated states at the $(k-1)$th step according to the difference between the actual measurement $\boldsymbol{Z}$ and the predicted measurement vector $\hat{\boldsymbol{Z}}_k$, and Kalman gain $\bar{\boldsymbol{K}}_k$ is defined as follows

$$\bar{\boldsymbol{K}}_k = \hat{\boldsymbol{P}}_{k-1}\boldsymbol{H}_k^T\left(\boldsymbol{H}_k\hat{\boldsymbol{P}}_{k-1}\boldsymbol{H}_k^T + \boldsymbol{R}\right)^{-1} \tag{17}$$

where $\hat{\boldsymbol{P}}_k$ is the error covariance matrix in the kth step. The Jacobian matrix $\boldsymbol{H}_k$ contains the partial derivatives of the measurement function h with respect to the state $\boldsymbol{X}$. The objective is to estimate the state vector $\boldsymbol{X} = [x_s, y_s, V_g]$ given the measurement vector $\boldsymbol{Z}$ and covariance matrix $\boldsymbol{R}$. Note that the measurement vector $\boldsymbol{Z}$ in equation (14) does not have the subscript k because its $(N-1)$ components (difference in arrival times) can be considered constant once the AE signals have been acquired. The uncertainty of the measurement vector $\boldsymbol{Z}$ is modeled as a zero-mean white Gaussian noise with covariance matrix $\boldsymbol{R}$ with diagonal terms defined in equation (5)

$$\boldsymbol{R} = \begin{bmatrix} \sigma^2_{\Delta t_{m1}} & \cdots & 0 \\ \vdots & \ddots & \vdots \\ 0 & \cdots & \sigma^2_{\Delta t_{m(N-1)}} \end{bmatrix} \tag{18}$$

As discussed in the "Sensor weighting" section, σ_{ti} in equation (5) can be calculated using the reliability function defined in equation (12). Note that the Kalman gain in equation (17) is inversely related to $\boldsymbol{R}$. Therefore, the sensors with a higher SNR (i.e. with

smaller σ_t) are given more weight, and those with a smaller SNR (with larger σ_t) are given less weight. The EKF will iteratively correct a priori knowledge of the state vector $\hat{\boldsymbol{X}}$ and covariance matrix $\hat{\boldsymbol{P}}$, with respect to $\boldsymbol{Z}$ and $\boldsymbol{R}$. The iteration begins with the initialization of the state vector estimate $\hat{\boldsymbol{X}}_0$ and its covariance matrix $\hat{\boldsymbol{P}}_0$ as follows

$$\hat{\boldsymbol{X}}_0 = [\hat{x}_{s_0}, \hat{y}_{s_0}, \hat{V}_{g_0}] \tag{19a}$$

$$\hat{\boldsymbol{P}}_0 = \begin{bmatrix} \sigma^2_{x_{s_0}} & 0 & 0 \\ 0 & \sigma^2_{y_{s_0}} & 0 \\ 0 & 0 & \sigma^2_{V_{g_0}} \end{bmatrix} \tag{19b}$$

It should be observed that for large values of A_{max}/σ_n, the probability of detection approximately tends to 1 and σ_t converge to zero; therefore, singularities may occur in the EKF algorithm. To overcome this limitation, it is proposed in this work to fix $\sigma_{ti} = 1$ μs as $A_{max}/\sigma_n > 8$. In fact, in the case of a sufficiently high SNR, each sensor's data can be treated equally.[15]

Initiation of location

The starting estimates of the AE source location $\hat{x}_{s_0}$ and $\hat{y}_{s_0}$ in equation (19a) can be calculated by geometrical considerations. Given an arbitrary group of N sensors at locations (x_i, y_i), it can be assumed that the estimated coordinates of the source location $\hat{x}_s$ and $\hat{y}_s$ can take any value in the intervals of (x_{sL}, x_{sU}) and (y_{sL}, y_{sU}), where x_{sL} and y_{sL} are the lower bounds defined as

$$x_{sL} = min\left([x_i]_N\right); y_{sL} = min\left([y_i]_N\right) \tag{20}$$

and x_{sU} and y_{sU} are the upper bounds defined as

$$x_{sU} = max\left([x_i]_N\right); y_{sU} = max\left([y_i]_N\right) \tag{21}$$

Under these assumptions, the mean and variance for an uncorrelated uniform distribution can be expressed as follows

$$\hat{x}_{s_0} = \frac{(x_{sU} + x_{sL})}{2}, \hat{y}_{s_0} = \frac{(y_{sU} + y_{sL})}{2} \tag{22}$$

$$\sigma^2_{x_{s_0}} = \frac{1}{12}(x_{sU} - x_{sL})^2, \sigma^2_{y_{s_0}} = \frac{1}{12}(y_{sU} - y_{sL})^2 \tag{23}$$

Initiation of group velocity

The starting estimates of the group wave velocity $\hat{V}_{g_0}$ and its variance $\sigma^2_{V_{g_0}}$ in equation (19b) can be calculated by equation (3). In particular, assuming f_i as the frequency corresponding to the maximum amplitude of the fast fourier transform (FFT) of the signal received (y_i), its velocity V_{g_i} can be obtained from the dispersion curves defined by equation (3) as follows
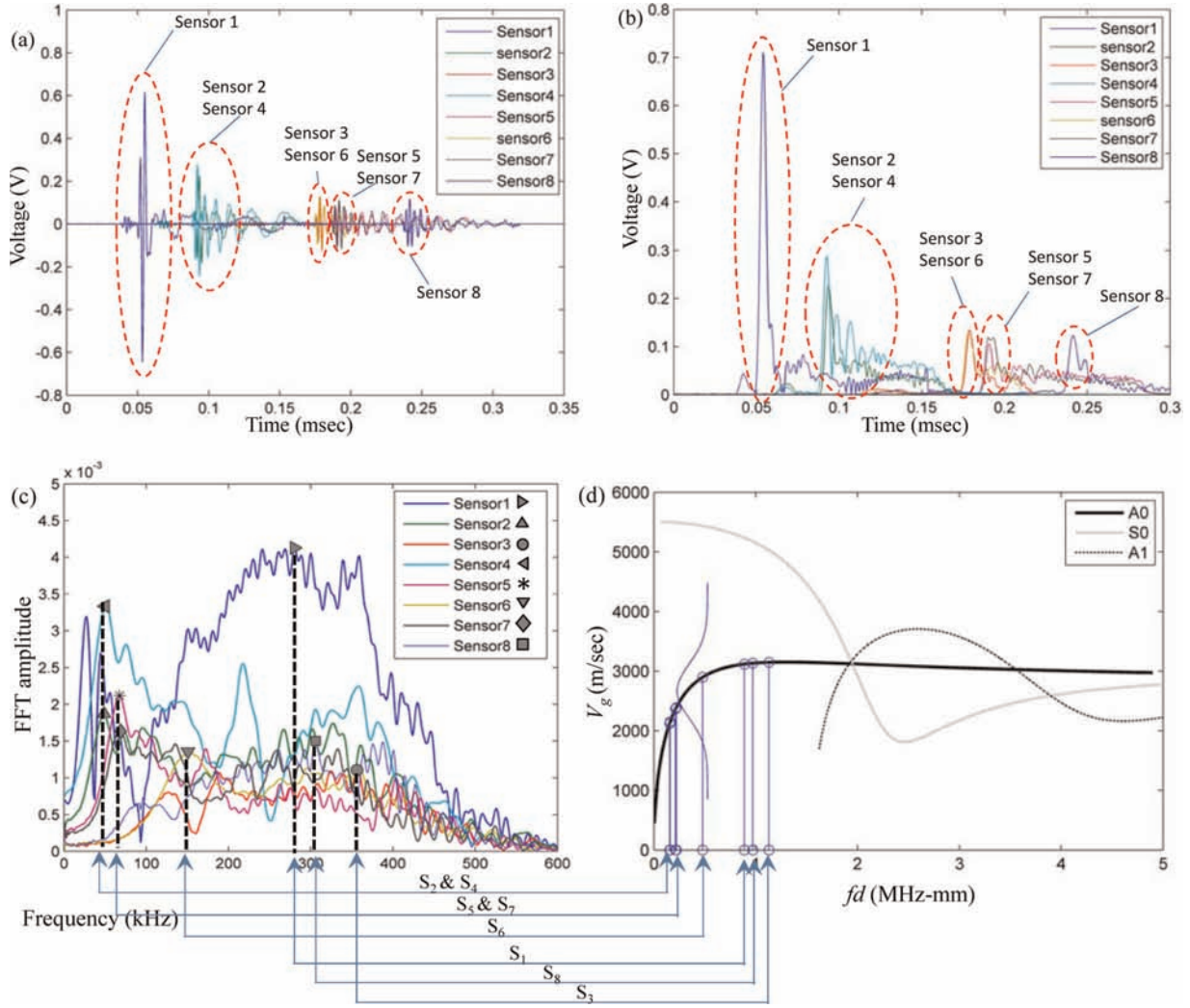
Figure 12. (a) Time history of recorded AE signals for eight sensors without artificial additive Gaussian noise, (b) signals envelope using Hilbert Transform, (c) FFT of recorded signals and the dominant frequencies, and (d) initiation of group wave velocity of Lamb mode A_0.

$$V_{g_i} = F(f_i d) \quad (24)$$

Therefore, given a sparse array of N sensors, the initial group wave velocity $\hat{V}_{g_0}$ is calculated as the average of the velocity (V_{g_i}), that is

$$\hat{V}_{g_0} = \bar{V}_g = \frac{\sum_{1}^{N} V_{g_i}}{N} \quad (25)$$

and the variance $\sigma^2_{V_{g_0}}$ as

$$\sigma^2_{V_{g_0}} = \frac{\sum_{1}^{N} \left(V_{g_i} - \bar{V}_g\right)^2}{N} \quad (26)$$

For the sake of clarity, Figures 12 shows this procedure for an array of eight sensors.

In particular, Figure 12(a) shows the time waveforms generated by a pencil lead break on the surface of an aluminum plate. Figure 12(b) shows the envelope for each signal, and in Figure 12(c) and (d), the FFT and the corresponding velocity (V_{g_i}) through the dispersion curves are depicted. In this work, the fundamental antisymmetric mode (A_0) has been assumed as the dominant Lamb wave mode. Overall, the proposed approach consists of four main stages as shown in the flowchart in Figure 13. The initial wave velocity distribution is just an initial guess to begin the algorithm. Indeed, the wave velocity of propagating waves will be estimated at the end of the iteration. The estimated
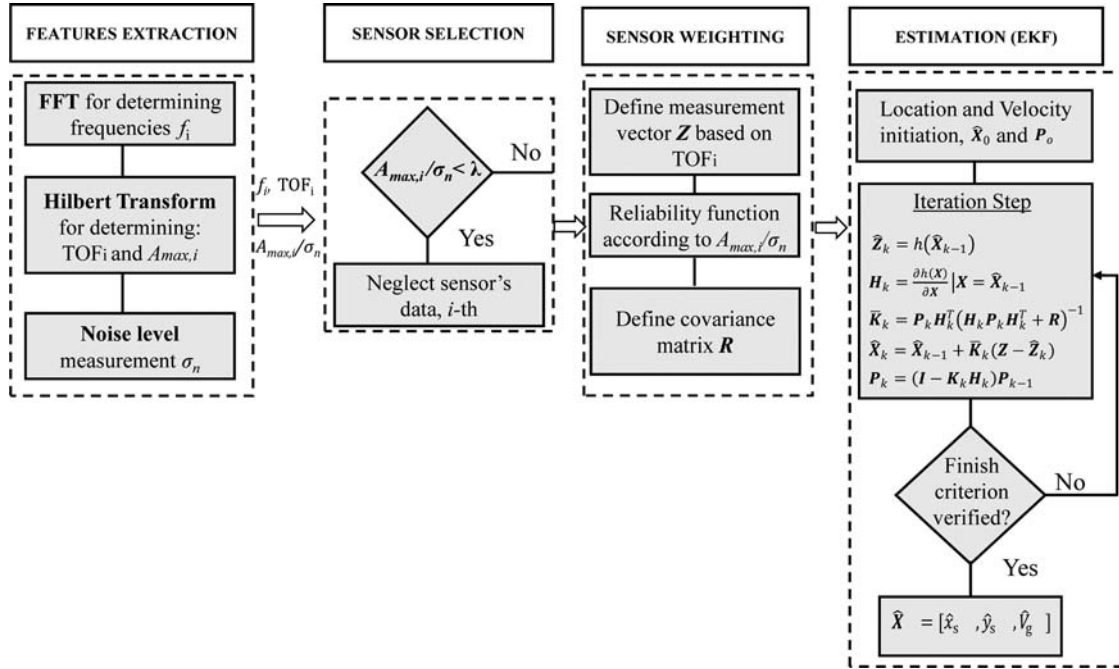
Figure 13. Proposed approach flowchart.
EKF: extended Kalman filter; TOF: time of flight.

wave velocity is the average velocity of propagating wave packet to reach each sensor that corresponds to the related measured TOF of the sensor.

The first stage (i.e. feature extraction) provides information about the TOF_i, dominant frequencies (f_i), peak amplitude of the signal envelope (A_{max}), and noise level (σ_n); during the second and third stages (i.e. sensor selection and sensor weighting), these features are used to eliminate and/or weight the sensor's data as discussed in the "Sensor selection based on binary hypothesis testing" and "Sensor weighting" sections; finally, the last stage of the process (i.e. estimation) uses the remaining sensor data and a priori information about the states, to iteratively estimate the state vector according to the measured information obtained during the second stage. The recursive procedure stops when a suitable finish condition is met; the elements of the state vector $\hat{X}$ corresponding to the last state estimate give the desired parameters of the AE location. In particular, to set the finish criterion, two approaches can be used as follows: (a) a minimum number of iterations can be fixed or (b) a value can be defined as the modulus of the difference between the state vector estimates provided by two consecutive Kalman filtering loops, that is

$$\text{Finish Criterion} = \left\| \hat{X}_k - \hat{X}_{k-1} \right\|_1 \quad (27)$$

This value is compared to a proper threshold value (empirical tests suggest a value of 10^{-5}). If the

difference is lower than the threshold, the recursive procedure stops, and the best estimate of the three parameters is delivered; otherwise, a new Kalman filtering loop is executed. In equation (27), $\|\ \|_1$ denotes the norm one.
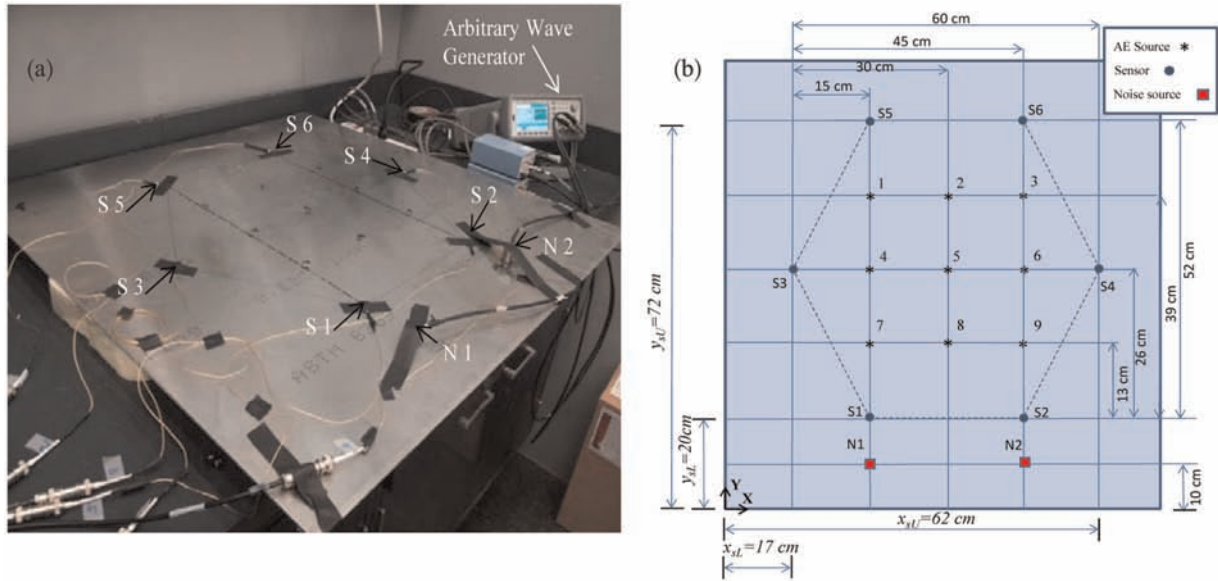
Experimental setup

The experiments were carried out using an aluminum plate with dimensions of 910 mm $\times$ 910 mm $\times$ 3.175 mm to validate the proposed algorithm. Two different experimental setups were used. In the first setup, an array of eight piezoelectric transducers in a square configuration with 560 mm dimension was used, as shown in Figure 14. In the second setup, six sensors in hexagonal configuration with the edge of 300 mm were used, as shown in Figure 15. Each sensor was connected to a preamplifier. For the data acquisition, an eight-channel high-speed data acquisition board (Physical Acoustics Corporation Micro-II PAC) with a sampling frequency of 3 MHz and dedicated software for signal processing and storage (AE_{win}) were used. During testing, the AE sources were generated by pencil lead breaks at systematic grid locations. To preferentially generate the antisymmetric (A_0) Lamb wave mode, the lead was fractured on the plate surface.[42] Postprocessing of the received signals was performed with a personal computer (PC) running a MATLAB software code implemented by the authors. Figures 14(b) and 15(b) show the schematic experimental setup. In these figures, the
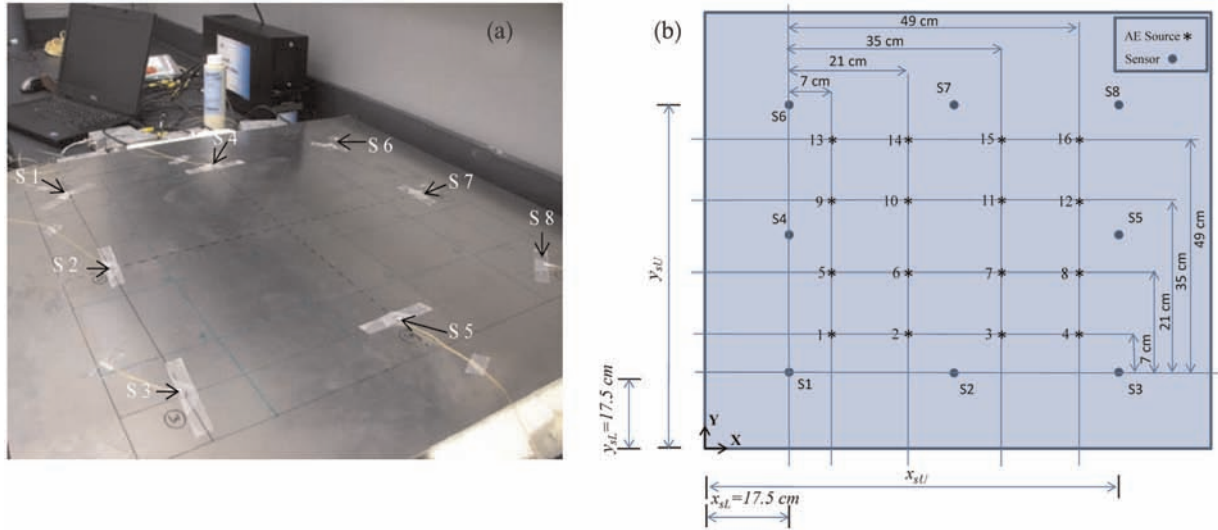
Figure 14. (a) The first experimental setup and (b) actual locations of simulated AE source with pencil lead break.

Figure 15. (a) The second experimental setup and (b) actual locations of simulated AE source with pencil lead break.

actual source location is marked with an asterisk (*) and each sensor is marked with a circle (○). In the first setup (Figure 14), the lower bounds x_{sL} and y_{sL} are the location of sensor 1, and the upper bounds x_{sU} and y_{sU} are the location of sensor 8. In the second experimental setup (Figure 15), the lower bounds x_{sL} and y_{sL} are the location of sensors 3 and 1, respectively, and the upper bounds x_{sU} and y_{sU} are the location of sensors 4 and 6, respectively.

The noise in the first experimental setup was simulated by artificially corrupting the acquired signals with additive Gaussian random noise. However, to simulate more realistic situation, in the second setup, two sources of noise were applied using two piezoelectric

transducers generating continuously high level of white noise by a two-channel arbitrary waveform generator during the pencil lead breaks, as shown in Figure 15. The bandwidths of the piezoelectric transducers for noise generation were 60 and 150 kHz and were used as the first and second noise sources, respectively.

Results and discussion

In both experimental setups, the proposed algorithm was applied in two modes as follows: (a) *regular multisensor fusion* and (b) *adaptive multisensor fusion*. In the first mode (i.e. regular multisensor fusion), each

sensor's information has been equally used (i.e. σ_t was fixed to 1 μs).[15] In the second mode (i.e. adaptive multisensor fusion), the probability of false alarm (P_F) in the selection stage was fixed to $\alpha = 0.04$, which corresponds to a threshold $\lambda = 4$ (i.e. solving equation (11)).

Artificial noise simulation (first experimental setup)

To validate the proposed algorithm, three levels of noise $\sigma_n = 0.03$, 0.04, and 0.05 were considered. Each generated AE signal (i.e. generated by a pencil lead break) was corrupted by an additive zero-mean Gaussian noise with one noise level using a Monte Carlo simulation. In particular, 1000 simulations were conducted for each actual location, and the estimated locations using the proposed algorithm were plotted. Figure 16 shows the estimated AE source locations using the "regular multisensor fusion algorithm" and the "adaptive multisensor fusion algorithm." The improvement obtained as a result of the adaptive procedure for all points and for different noise levels is clearly observed. Note that large errors were observed in some points (i.e. 1, 4, 13, and 16) due to multiple reflections from the plate edges.

To evaluate this algorithm quantitatively, an error ε_{r_i} is defined for each estimated point as follows

$$\varepsilon_{r_i} = \sqrt{\left(x_s - \hat{x}_{s_i}\right)^2 + \left(y_s - \hat{y}_{s_i}\right)^2} \qquad i = 1, \ldots, N_s \quad (28)$$

where N_s is the number of simulations. The statistics of the error ε_r, mean and standard deviation, are defined as follows

$$\overline{\varepsilon_r} = \frac{\sum_1^{N_s} \varepsilon_{r_i}}{N_s} \tag{29}$$

$$\sigma^2_{\varepsilon_r} = \frac{\sum_1^{N_s} \left(\varepsilon_{r_i} - \overline{\varepsilon_r}\right)^2}{N_s} \tag{30}$$

The most desirable estimator is one with the lowest mean (unbiased) and standard deviation of error. Figure 17 shows the mean and standard deviation defined in equations (29) and (30) for the two modes and noise levels considered. It can be observed that good improvements are achieved in terms of the mean and standard deviation of estimation error at any point. The computational cost of the proposed algorithm, using a regular PC, is less than 0.03 s for each point. Table 1 summarizes the average of the mean and standard deviation of radius of error for 16 points for each noise level.

Real noise simulation (second experimental setup)

To validate the proposed algorithm in a more realistic noisy environment, two piezoelectric transducers were used in the second experimental setup (see Figure 15) to continuously generate two white noise signals by a two-channel arbitrary waveform generator. The amplitude of the two signals was 0.1-V peak to peak. The transducers were connected to two 40-dB amplifiers. The generated noise bandwidth of the first (60 kHz bandwidth transducer) and second (150 kHz bandwidth transducer) sources was set to 20 and 200 kHz, respectively, to simulate both high and low bandwidth noises. Ten pencil lead breaks were conducted ($N_s = 10$) on each point, and the signals were stored in a PC for postprocessing. It should be mentioned that using an artificial noise, the information of the noise level is a priori knowledge for each sensor; however, in a real situation, the level of noise has to be measured for each sensor. The level of the background noise σ_n for each sensor was measured by calculating the RMS value of a predetermined portion of the signal before the first arrival of each signal, so that obviously the level of the noise for each sensor is different. Figure 18 shows the estimated AE source locations using the "regular multisensor fusion algorithm" and the "adaptive multisensor fusion algorithm." The improvement obtained as a result of the adaptive procedure for all points in real noisy environment is clearly observed (note that for clarity in Figure 18, each estimated location is connected with a line to the actual corresponding source location). Figure 19 shows the mean and standard deviation defined in equations (29) and (30) in the two modes for real noise simulation. The significant error reduction in terms of mean and standard deviation of radius of error was achieved.

Table 2 summarizes the average of the mean and standard deviation of radius of error for nine-point real noise simulation. It is worth noting that in the second experimental setup due to high level of noise, a commercially available AE software could not even properly operate as a result of many false alarms or miss detections.

Conclusion

In this article, an adaptive multisensor fusion algorithm for locating the AE sources in noisy operational conditions is proposed. Based on a fixed probability of false alarm, a threshold has been calculated to eliminate the data from unreliable sensors using the *Neyman–Pearson* test. Then, the remaining data sensors were weighted based on a predetermined reliability function that correlates the ratio between the peak amplitude of the signal envelope and noise level, to uncertainty of the TOF measurement. Finally, the remaining weighted data are fed into an estimation procedure based on the EKF.
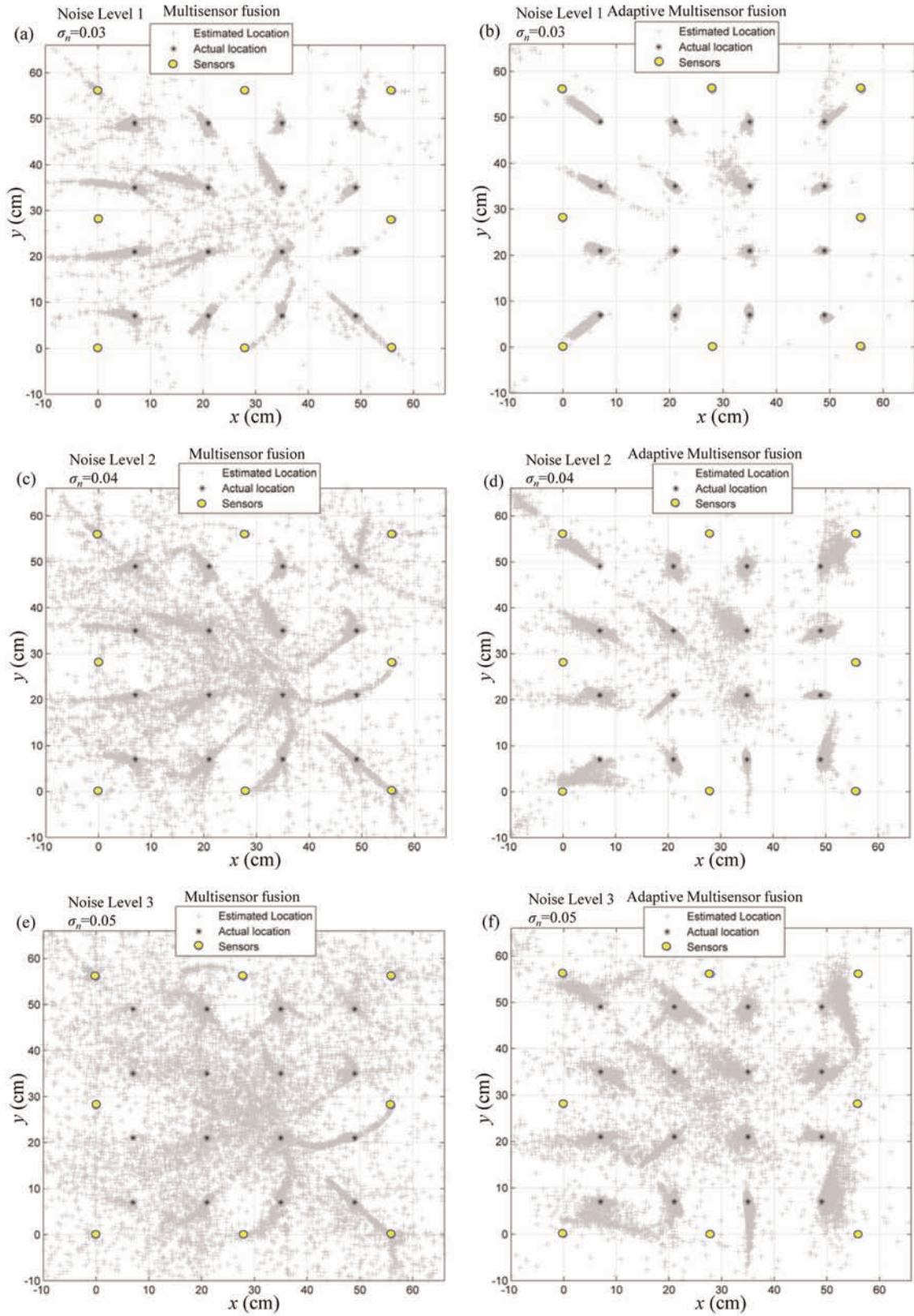
Figure 16. Actual and estimated locations for 16 simulated AE sources for 1000 Monte Carlo simulations using: (a) noise level 1 and regular sensor fusion, (b) noise level 1 and adaptive sensor fusion, (c) noise level 2 and regular sensor fusion, (d) noise level 2 and adaptive sensor fusion, (e) noise level 3 and regular sensor fusion, and (f) noise level 3 and adaptive sensor fusion.
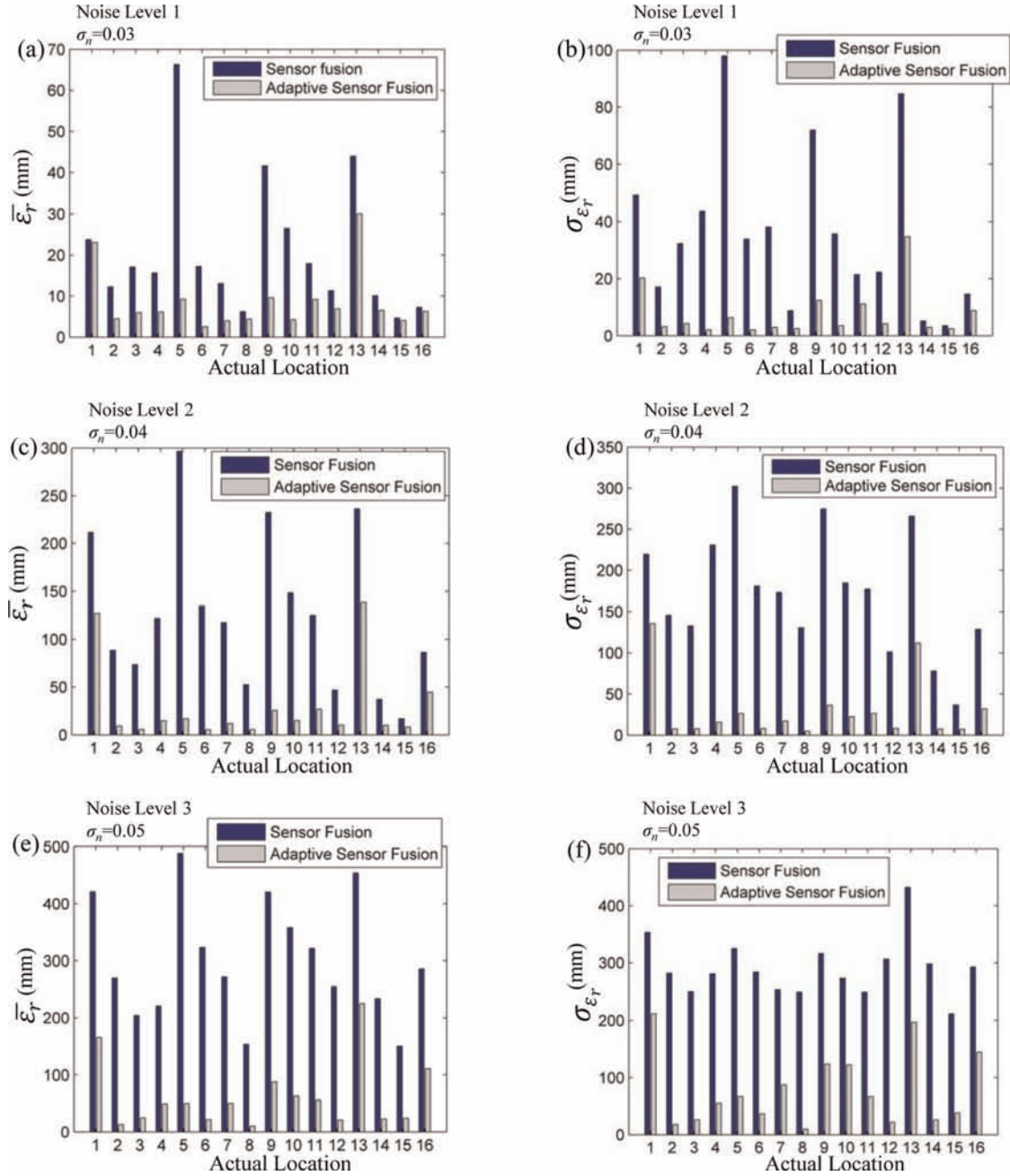
Figure 17. Mean and standard deviation of error ε_r for regular sensor fusion and adaptive sensor fusion: (a) noise level 1 and mean of ε_r; (b) noise level 1 and standard deviation of ε_r; (c) noise level 2 and mean of ε_r; (d) noise level 2 and standard deviation of ε_r; (e) noise level 3 and mean of ε_r; and (f) noise level 3 and standard deviation of ε_r.

The main advantages of the proposed algorithm are given as follows: (a) flexibility in fusion of the data due to the matrix structure of the estimation stage, (b) accurate AE source localization in noisy environments, and (c) the computation cost makes it feasible for real-time applications.

Table 1. Average of mean $\bar{\varepsilon}_r$ and standard deviation σ_{ε_r} error for 16 points with total 16 × 1000 simulations for each noise level

Noise level	Average of mean error $\bar{\varepsilon}_r$ (mm)		Average of STD error σ_{ε_r} (mm)	
	Multisensor	Adaptive multisensor	Multisensor	Adaptive multisensor
Level 1 (σ_n = 0.03)	20.92	8.56	36.26	7.74
Level 2 (σ_n = 0.04)	126.58	29.57	172.66	29.69
Level 3 (σ_n = 0.05)	301.68	61.85	291	78.21
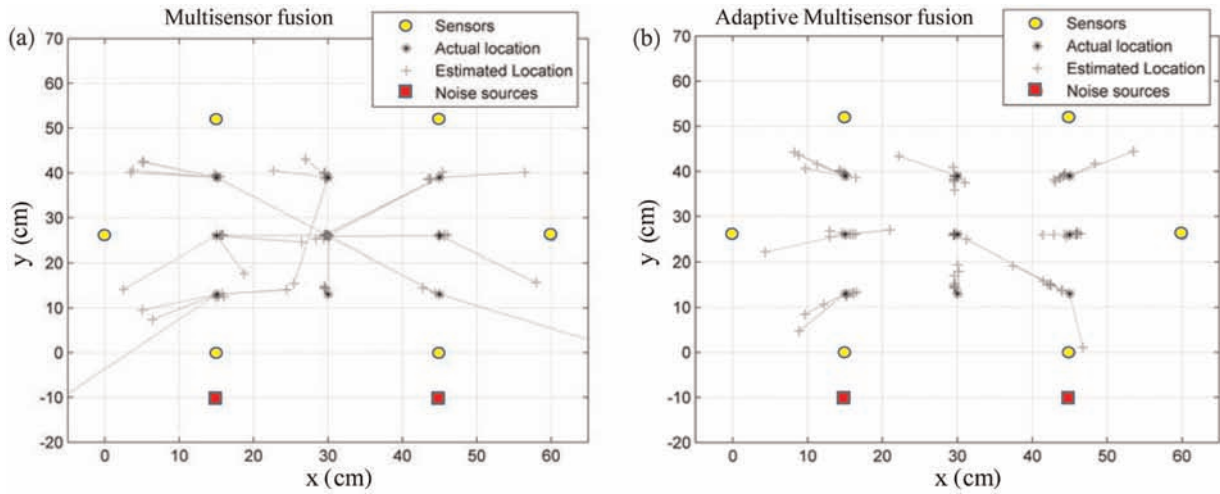
Figure 18. Actual and estimated locations for nine simulated AE sources for 10 pencil lead breaks and real noise simulations using (a) regular sensor fusion and (b) adaptive sensor fusion.
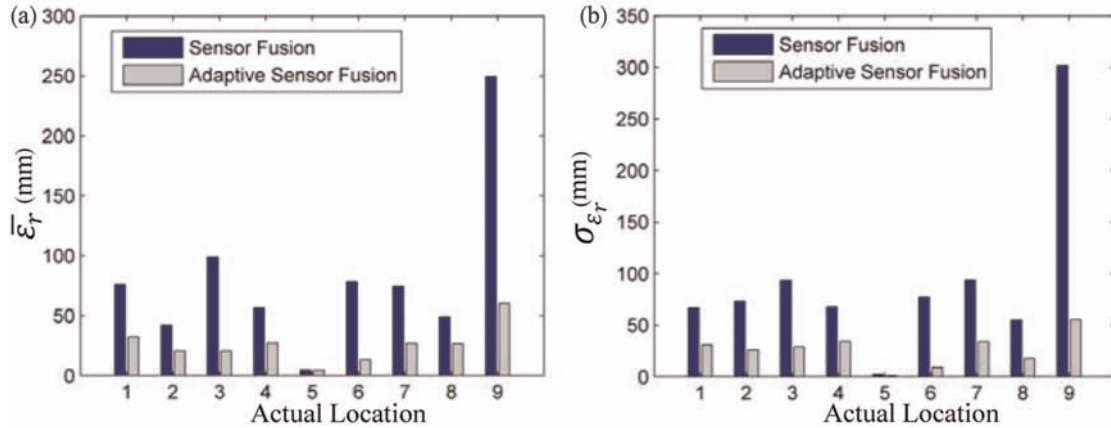
Figure 19. Mean and standard deviation of error ε_r for regular sensor fusion and adaptive sensor fusion: (a) mean of ε_r and (b) standard deviation of ε_r.

Table 2. Average of mean $\bar{\varepsilon}_r$ and standard deviation σ_{ε_r} error for nine points with total 9 × 10 pencil lead breaks for real noise

	Average of mean error $\bar{\varepsilon}_r$ (mm)		Average of standard deviation error σ_{ε_r} (mm)	
	Multisensor	Adaptive multisensor	Multisensor	Adaptive multisensor
Automatic noise level detection	81.05	25.78	92.36	26.39

References

1. Tan K. Comparison of Lamb waves and pulse echo in detection of near-surface defects in laminate plates. *NDT & E Int* 1995; 28: 215–223.
2. Ghosh T, Kundu T and Karpur P. Efficient use of Lamb modes for detecting defects in large plates. *Ultrasonics* 1998; 36: 791–801.
3. Tua PS, Quek ST and Wang Q. Detection of cracks in plates using piezo-actuated Lamb waves. *Smart Mater Struct* 2004; 13: 643–660.
4. Staszewski W, Boller C and Tomlinson G. *Health monitoring of aerospace structures smart sensor technologies and signal processing*. England: John Wiley & Sons, 2004.
5. Giurgiutiu V and Bao J. Embedded-ultrasonics structural radar for in-situ structural health monitoring of thin-wall structures. *Struct Health Monit* 2004; 3: 121–140.
6. Su Z and Ye L. Fundamental Lamb mode-based delamination detection for CF/EP composite laminates using distributed piezoelectrics. *Struct Health Monit* 2004; 3: 43–68.
7. Mal A, Ricci F, Banerjee S, et al. A conceptual structural health monitoring system based on vibration and wave propagation. *Struct Health Monit* 2005; 4: 283–293.
8. Kundu T, Das S and Jata KV. Point of impact prediction in isotropic and anisotropic plates from the acoustic emission data. *J Acoust Soc Am* 2007; 122: 2057–2066.
9. Kundu T, Das S, Martin SA, et al. Locating point of impact in anisotropic fiber reinforced composite plates. *Ultrasonics* 2008; 48: 193–201.
10. Salamone S, Bartoli I, Leo PD, et al. High-velocity impact location on aircraft panels using macro-fiber composite piezoelectric rosettes. *J Intell Mater Syst Struct* 2010; 21: 887–896.
11. Marchi LD, Marzani A, Speciale N, et al. A passive monitoring technique based on dispersion compensation to locate impacts in plate-like structures. *Smart Mater Struct* 2011; 20: 035021.
12. Jeong H and Jang YS. Fracture source location in thin plates using the wavelet transform of dispersive waves. *IEEE Trans Ultrason Ferroelectr Freq Control* 2000; 47: 612–619.
13. Ciampa F and Meo M. Acoustic emission source localization and velocity determination of the fundamental mode A0 using wavelet analysis and a Newton-based optimization technique. *Smart Mater Struct* 2010; 19: 045027.
14. Dehghan Niri E and Salamone S. A probabilistic framework for acoustic emission (AE) source localization in plate-like structures. *Smart Mater Struct* 2012; 21: 035009.
15. Dehghan Niri E, Salamone S and Singla P. Acoustic emission (AE) source localization using extended Kalman filter (EKF). *Proc. SPIE 8348*, Health Monitoring of Structural and Biological Systems 2012, 834804 (April 26, 2012). DOI:10.1117/12.914848.
16. Lu Y and Michaels JE. A methodology for structural health monitoring with diffuse ultrasonic waves in the presence of temperature variations. *Ultrasonics* 2005; 43: 717–731.
17. Konstantinidis G, Drinkwater BW and Wilcox PD. The temperature stability of guided wave structural health monitoring systems. *Smart Mater Struct* 2006; 15: 967–976.
18. Croxford AJ, Wilcox PD, Drinkwater BW, et al. Strategies for guided-wave structural health monitoring. *Proc R Soc A* 2007; 463: 2961–2981.
19. Lanza di Scalea F and Salamone S. Temperature effects in ultrasonic Lamb wave structural health monitoring systems. *J Acoust Soc Am* 2008; 124: 161–174.
20. Salamone S, Bartoli I, Lanza di Scalea F, et al. Guided-wave health monitoring of aircraft composite panels under changing temperature. *J Intell Mater Syst Struct* 2009; 20: 1079–1090.
21. Clarke T, Simonetti F and Cawley P. Guided wave health monitoring of complex structures by sparse array systems: influence of temperature changes on performance. *J Sound Vib* 2010; 329: 2306–2322.
22. Marioli D, Narduzzi C, Offelli C, et al. Digital time of flight measurement for ultrasonic sensors. In: *Instrumentation and measurement technology conference, IMTC-91*. Conference Record., 8th IEEE Atlanta, Georgia, 14–16 May 1991, pp.198–201.
23. Andria G. Digital signal processing techniques for accurate ultrasonic sensor measurement. *Measurement* 2001; 30: 105–114.
24. Seydel R and Chang FK. Impact identification of stiffened composite panels: I. System development. *Smart Mater Struct* 2001; 10: 354–369.
25. Haywood J, Coverley PT, Staszewski W, et al. An automatic impact monitor for a composite panel employing smart sensor technology. *Smart Mater Struct* 2005; 14: 265–271.
26. Leclerc J, Worden K, Staszewski W, et al. Impact detection in an aircraft composite panel—a neural-network approach. *J Sound Vib* 2007; 299: 672–682.
27. Ing RK, Quieffin N, Catheline S, et al. In solid localization of finger impacts using acoustic time-reversal process. *Appl Phys Lett* 2005; 87: 204104.
28. Sohn H, DeSimio M P, Olson S E, et al. Impact localization in an aircraft fuselage using laser based time reversal. *Proc. SPIE 7984*, Health Monitoring of Structural and Biological Systems 2011, 79841G (March 31, 2011). DOI:10.1117/12.881912.
29. Park B, Sohn H, Olson SE, et al. Impact localization in complex structures using laser-based time reversal. *Structural Health Monitoring* 2012 First published on July 1, 2012. DOI:10.1177/1475921712449508.
30. Ciampa F and Meo M. Impact detection in anisotropic materials using a time reversal approach. *Struct Health Monit* 2011; 11: 43–49.
31. Kundu T, Das S and Jata KV. Detection of the point of impact on a stiffened plate by the acoustic emission technique. *Smart Mater Struct* 2009; 18: 035006.
32. Hajzargarbashi T, Kundu T and Bland S. An improved algorithm for detecting point of impact in anisotropic inhomogeneous plates. *Ultrasonics* 2011; 51: 317–324.

33. Kundu T, Nakatani H and Takeda N. Acoustic source localization in anisotropic plates. *Ultrasonics* 2012; 52: 740–746.

34. Gaul L. Identification of the impact location on a plate using wavelets. *Mech Syst Signal Process* 1998; 12: 783–795.

35. Gaul L, Hurlebaus S and Jacobs L. Localization of a synthetic acoustic emission source on the surface of a fatigue specimen. *Res Nondestruct Eval* 2001; 13: 105–117.

36. Coverley PT and Staszewski W. Impact damage location in composite structures using optimized sensor triangulation procedure. *Smart Mater Struct* 2003; 12: 795–803.

37. Dasarathy BV. Sensor fusion potential exploitation—innovative architectures and illustrative applications. *Proc IEEE* 1997; 85: 24–38.

38. Hall DL and Llinas J. An introduction to multisensor data fusion. *Proc IEEE* 1997; 85: 6–23.

39. Gros XE. *Applications of NDT data fusion*. Massachusetts, USA: Kluwer Academic Publishers, 2001.

40. Auld BA. *Acoustic fields and waves in solids*. New York: Wiley Interscience, 1973.

41. Soong TT. *Fundamentals of probability and statistics for engineers*. England: John Wiley & Sons Ltd, 2004.

42. Gorman MR and Prosser WH. AE source orientation by plate wave analysis. *J Acoust Emiss* 1991; 9: 283–288.

43. Wilcox PD. Lamb wave inspection of large structures using permanently attached transducers. PhD thesis, Imperial College of Science, Technology and Medicine, London, UK, 1998.

44. Banerjee S, Mal AK and Prosser WH. Analysis of transient Lamb waves generated by dynamic surface sources in thin composite plates. *J Acoust Soc Am* 2004; 115: 1905–1911.

45. Viktorov IA. *Rayleigh and Lamb waves: physical theory and applications*. New York: Plenum Press, 1967.

46. Wilcox PD, Cawley P and Lowe MJS. Acoustic fields from PVDF interdigital transducers, science measurement and technology. *Proc IEEE* 1998; 145: 250–259.

47. Van der Heijden F, Duin RPW, De Ridder D, et al. *Classification, parameter estimation, and state estimation*. England: John Wiley & Sons Ltd, 2004.

48. Parrilla M, Anaya JJ and Fritsch C. Digital signal processing techniques for high accuracy ultrasonic range measurements. *IEEE Trans Instrum Meas* 1991; 40: 759–763.

49. Trees HLV. *Detection, estimation, and modulation theory: part I*. New York, USA: John Wiley & Sons, 2001.

50. Park JH and Kim YH. Impact source localization on an elastic plate in a noisy environment. *Smart Mater Struct* 2006; 17: 2757–2766.

51. Crassidis JL and Junkins JL. *Optimal estimation of dynamic systems*, Boca Raton, FL, USA: Chapman & Hall/CRC, 2004.

52. Zarate BA, Caicedo JM, Yu J, et al. Bayesian model updating and prognosis of fatigue crack growth. *Eng Struct* 2012; 45: 53–61.

53. Sabatini AM. A digital signal-processing technique for compensating ultrasonic sensors. *IEEE Trans Instrum Meas* 1995; 44: 869–874.

54. Tsai CC. A localization system of a mobile robot by fusing dead-reckoning and ultrasonic measurements. *IEEE Trans Instrum Meas* 1998; 47: 1399–1404.

55. Moreno VM and Pigazo A. *Kalman filter: recent advances and applications.* InTech, 2009.